

## Nanoscale

# Graphene-coated Nickel in Biological Environments: Role of Structural Defects

Journal:	Nanoscale
Manuscript ID	NR-ART-01-2024-000280.R1
Article Type:	Paper
Date Submitted by the Author:	11-Aug-2024
Complete List of Authors:	Devadig, Ramesh; South Dakota School of Mines and Technology Sigdel, Pawan; South Dakota School of Mines and Technology Rahman, Md. Hasan-Ur; South Dakota School of Mines and Technology Ajayan, Pulickel; Rice University, Mechanical Engineering and Materials Science Rahman, Muhammad; Rice University, Materials Science and NanoEngineering Gadhamshetty, Venkataramana; South Dakota School of Mines and Technology

SCHOLARONE™ Manuscripts Page 1 of 33 Nanoscale

## **Graphene-coated Nickel in Biological Environments: Role of Structural Defects**

Ramesh Devadig<sup>1,2,3</sup>, Pawan Sigdel<sup>1,2,3</sup>, Md. Hasan-Ur Rahman<sup>1,2,3</sup>, Pulickel M. Ajayan<sup>4\*</sup>, Muhammad M. Rahman<sup>4\*</sup>, Venkataramana Gadhamshetty<sup>1,2,3\*</sup>

<sup>1</sup>Civil and Environmental Engineering, South Dakota Mines, 501 E. St. Joseph Street, Rapid City, SD, 57701, USA

<sup>2</sup>2D-materials for Biofilm Engineering, Science and Technology (2DBEST) Center, South Dakota Mines, 501 E. St. Joseph Street, Rapid City, SD, 57701, USA

<sup>3</sup>Data-Driven Materials Discovery for Bioengineering Innovation Center, South Dakota Mines, 501 E. St. Joseph Street, Rapid City, SD, 57701, USA

<sup>4</sup>Department of Materials Science and NanoEngineering, Rice University, Houston, TX 77030, USA

\*Corresponding Author: <u>ajayan@rice.edu</u> (Pulickel Ajayan), <u>maksud@rice.edu</u> (Muhammad M. Rahman), Venkata.Gadhamshetty@sdsmt.edu (Venkataramana Gadhamshetty)

Nanoscale Page 2 of 33

#### Abstract

Graphene (Gr) is a promising material for addressing microbially induced corrosion (MIC) issues that cause staggering economic losses, estimated at nearly \$55 billion annually in the US alone. However, structural defects including edges, grain boundaries, and cracks can compromise its performance in aggressive biological environments. Owing to the technological relevance of nickel (Ni), its key roles in biological mechanisms, and the strong hybridization of d-electrons of Ni with Gr  $\pi$ -orbitals, we explore the effects of the key defects in Gr/Ni exposed to archetype sulfate-reducing bacteria (SRB). Electrochemical and spectroscopy tests revealed that the grain boundaries play a stronger role than cracks. The edges and grain boundaries in as-grown Gr on Ni (dGr/Ni) aggravated corrosion by two-fold, while the cracks in the transferred counterpart that lacked these defects improved corrosion resistance by 2-fold. A combination of biotic and abiotic studies corroborated the unique roles of grain boundaries as sulfur reservoirs to promote the attachment of sessile SRB cells and subsequent redox reactions. Analysis of distinct biogenic products confirmed the role of grain boundaries on pitting corrosion. These insights can guide the rational design of graphene coatings specifically for biological environments prone to MIC.

**Keywords:** edges, defects, grain boundaries, graphene, sulfate-reducing bacteria

Page 3 of 33 Nanoscale

#### 1. Introduction

Owing to extreme thinness, long-range  $\pi$ -conjugation, and dense packing of an atom-thick planar sheet of sp2-bonded carbon atoms within a honeycomb crystal lattice, [1] graphene (Gr) serves as building blocks for atomically thin (< 4 nm) barrier coatings. [2] Such coatings find exciting uses in biosensors, [3] drug delivery, [4] bio-electrochemical systems, [5] tissue engineering, [6] enzyme immobilization, [7] and antimicrobial material. [8] Prior studies have explored Gr as a noninvasive coating for protecting metals against salt, chemicals, and microorganisms. [2,9,10] Gr materials show promise to serve as protective coatings against both abiotic corrosion [2,9,10] and microbially influenced corrosion (MIC), which jointly contributes to the annual estimated direct costs of nearly \$276 billion in the U.S. alone. [11] Nearly 20% of these costs are attributed to MIC, which is caused by sulfate-reducing bacteria (SRB). [12]

Established methods for the growth and processing of Gr materials can inadvertently introduce structural defects [13,14] that compromise their performance in biological environments. For instance, the chemical vapor deposition (CVD) of a monolayered Gr on Nickel (Ni) follows a precipitated growth process to yield Ni carbide interfaces and create isolated islands of Gr.<sup>[15]</sup> A lattice mismatch between Gr and Ni [16] during the CVD growth can yield chemically active defects [17] that attract dopants.<sup>[16,18]</sup> Grain boundaries (GBs) can impart structural inhomogeneities [19] to impose strain effects [16] and compromise the chemical, electrical, and mechanical properties of Gr coatings.<sup>[19]</sup> Wrinkles and cracks that originate during the transfer processes can influence the barrier properties.<sup>[20]</sup> Nickel-containing materials and their alloys are widely used,<sup>[21]</sup> such as stainless steel, lie at the heart of water purification, transport, collection, and wastewater disposal and are prone to corrosion. Thus, owing to the strong hybridization of

Nanoscale Page 4 of 33

the d-electrons of Ni with  $\pi$ -orbitals of Gr, the Gr/Ni provides an ideal interface<sup>[22]</sup> to analyze the effects of the above defects in biological environments.

Prior experimental studies on Gr/Ni or first principle theoretical studies on defect-mediated corrosion mechanisms of Gr mostly focused on abiotic environments. [2,14,16,23] Such baseline data is lacking for biological environments, which is valuable to train deep learning models for developing Gr coatings for biotechnology applications. [24–26] Given the key role in many engineering domains (e.g., electroplating, batteries, medical implants) this study focuses on unveiling the effects of structural defects on the behavior of Gr/Ni in aggressive biological environments imposed by MIC-causing SRB. Prior fundamental studies based on pure cultures of SRB have focused primarily on Gr/Cu interfaces [9,21] except for two isolated studies on Gr-coated Ni alloy [10] and Ni foam, [27] both of which used mixed microbial cultures containing SRB.

This study explores the relative effects of structural defects in as-grown and transferred forms of Gr on polycrystalline (PC) Ni exposed to pure cultures of SRB *Oleidesulfovibrio* alaskensis G20 (OA-G20, previously known as *Desulfovibrio alaskensis* G20). OA-G20 was chosen as a model SRB due to its genetically tractable nature and our familiarity with this strain. [9,28] Our specific goals are to (i) generate baseline data for defect-mediated MIC behavior of CVD-Gr and its transferred counterpart on PC-Ni; (ii) understand the relative influences of Gr edges (due to incomplete surface coverage), grain boundaries, and cracks in Gr on microbial interactions with the underlying Ni substrate. Abiotic studies were used to corroborate the mechanistic understanding of the effects of these defects. Leveraging these fundamental insights, we present a comprehensive analysis of the unique effects of defects on the performances of

Page 5 of 33 Nanoscale

Gr/Ni facing aggressive biotic environments (relative to chemical environments). This analysis serves as a basis for rationally designing and developing MIC-resistant Gr coatings.

Nanoscale Page 6 of 33

#### 2. Results and Discussion

## 2.1. Characterization of Gr coatings

The G Raman band (E<sub>2g</sub> vibration, 1584 cm<sup>-1</sup>) and 2D band (A<sub>1g</sub> vibration, 2781 cm<sup>-1</sup>) show signatures of Gr in both dGr/Ni and biGr/Ni, respectively (Figure 1a).<sup>[29]</sup> However, they feature different forms of defects. A distinct D-peak (1335 cm<sup>-1</sup>) in dGr/Ni shows the presence of intervalley defects [30] and breathing modes of six carbon atom rings, [31] armchair edge defects [32], and nonuniformity. [33] The dGr/Ni also displays greater defect density which is evident from its higher I<sub>D</sub>/I<sub>G</sub> ratio. The biGr/Ni lacks the D-peak. [32] The symmetric nature of the 2D peak and the  $I_G/I_{2D}$  ratio of 0.32 (<1.0)[34] reveals a monolayered Gr in dGr/Ni. The biGr/Ni features a bilayered Gr based on the values of 2D peak position ( $\sim$ 2700 cm<sup>-1</sup>) and  $I_G/I_{2D}$  ratio (1.01).<sup>[35]</sup> The surface coverage of Gr films on dGr/Ni and biGr/Ni were analyzed after transferring them onto SiO<sub>2</sub>/Si, respectively (Figure 1b-c, Figure S1). The dGr/Ni featured incomplete Gr coverage (64.5±15 %, Figure 1b) while biGr/Ni showed a conformal coating (Figure 1c) with coverage as high as 97.5±2 % (Figure 1d). The incomplete coverage of dGr/Ni was due to the formation of intermediate nickel carbide which is associated with the Gr growth during the chemical vapor deposition process. Gr growth on a Ni surface can be discontinuous due to the competition between graphene growth and the formation of a surface nickel carbide.[15] The presence of nickel carbide was confirmed through the presence of Raman signatures and Auger spectroscopy (Figure. S2). As a result, regions with incomplete Gr growth were not transferred onto Si/SiO<sub>2</sub> during the transfer process. Although, both the systems featured islands of Gr [36] (Figure 1b, Figure 1c), the areal footprint of these islands in dGr/Ni (2677±1420 µm²) was 7-fold greater than biGr/Ni (382.5±175 µm²). The island density for dGr/Ni (82±10 islands.mm<sup>-2</sup>) was also 7% greater than biGr/Ni (76±6 islands.mm<sup>-2</sup>) (Figure 1d). It should be noted that in both cases, the Gr islands were composed of monolayer Gr. However, dGr/Ni featured discontinuous (isolated)

Page 7 of 33 Nanoscale

Gr islands, which affected the surface coverage of dGr/Ni. In contrast, while biGr/Ni also featured monolayer Gr islands, they were connected to the bilayered Gr, thereby not affecting the surface coverage of biGr/Ni.

The dGr/Ni also featured a greater number of GBs than biGr/Ni (CLSM and SEM images, Figure 1e-f) which can be attributed to the annealing step during the CVD growth. [37] These GBs ranged from 10 to 40  $\mu$ m (see Figure 1f). The AFM topographic height images of these GBs (featuring the edges) in dGr/Ni showed 550 nm and -550.1 nm as the highest and lowest points, respectively (Figure 1g). The greater number of GBs and their varying sizes imparted greater roughness to dGr/Ni. The dGr/Ni and biGr/Ni were 25% and 10% rougher compared to bare Ni respectively, based on root mean square height (Sq) (see CLSM images). This result was corroborated after observing the greater arithmetic mean height (Sa) for dGr/Ni (Figure 1h). The biGr/Ni (<3%) was blemished by the presence of cracks (Figure 1c). The contact angles of both dGr/Ni (66.5  $\pm$  3.5°) and biGr/Ni (80.2  $\pm$  5.9°) were lower than bare Ni (106.6  $\pm$  6.1°) (Figure 1i). This indicates that the Gr coatings improve the wettability of Ni substrates. [38]

Nanoscale Page 8 of 33

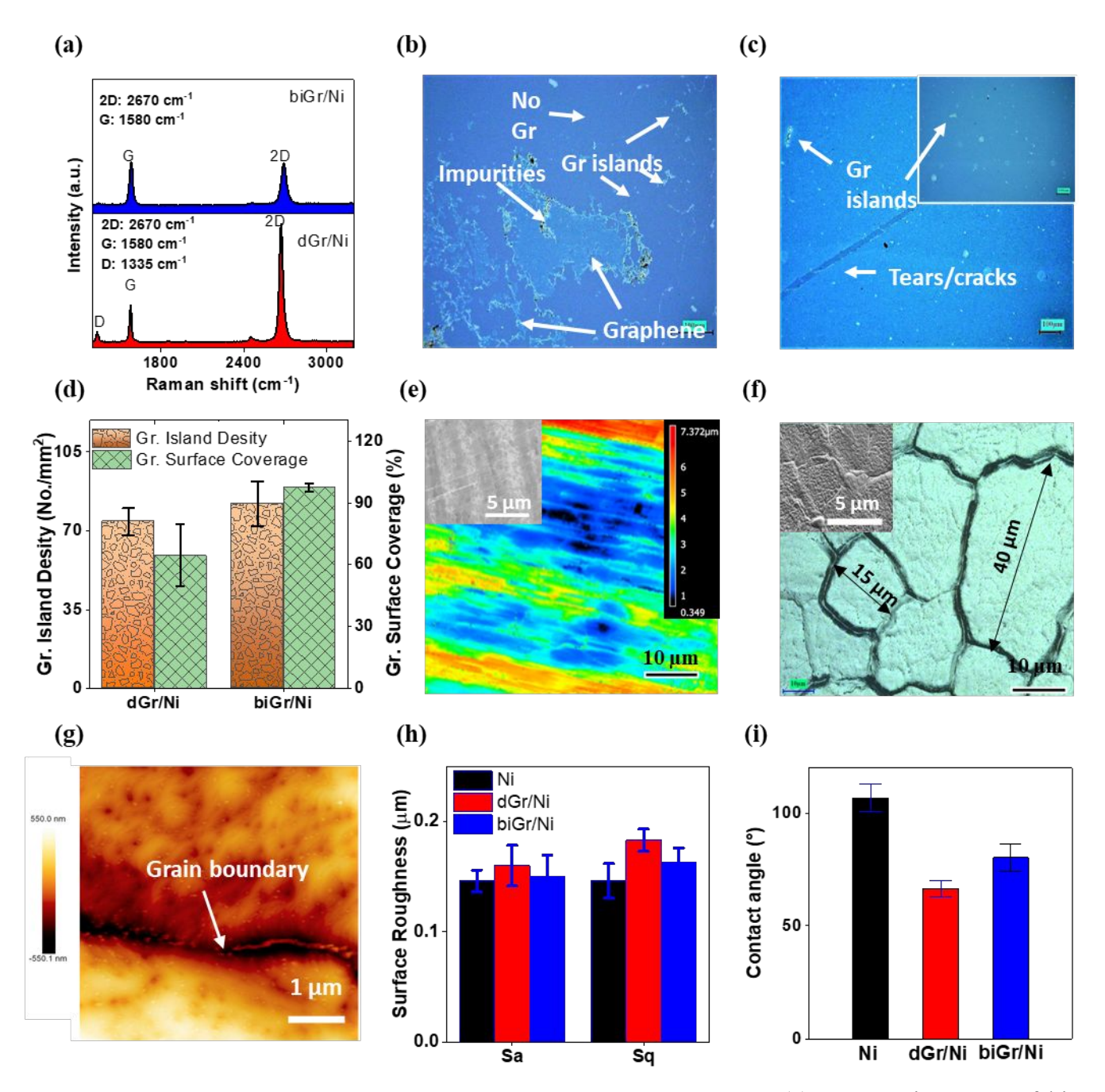


**Figure 1. Characterization of bare Ni, dGr/Ni, and biGr/Ni.** (a) Raman signatures of bilayered graphene (top stack) and monolayered graphene (bottom stack) on  $SiO_2/Si$ . (b) Optical images of dGr transferred onto  $SiO_2/Si$  (Scale bar  $100\mu m$ ). (c) Optical images of biGr transferred onto  $SiO_2/Si$  (Inset: graphene islands) (Scale bar  $100\mu m$ ). (d) The island density and surface coverage of Gr in dGr/Ni and biGr/Ni (e) CLSM height images for biGr/Ni (Inset: SEM image of biGr/Ni) (f) CLSM image of dGr/Ni showing grain boundaries (GBs) (Inset: SEM image of dGr/Ni) (g) AFM image of dGr/Ni showing the surface roughness across the GBs (h) Temporal variation of surface roughness in bare Ni, dGr/Ni and biGr/Ni (i) Contact angle measurement showing the hydrophobic nature of bare Ni and hydrophilic nature of coated samples, respectively. All experiments were conducted in triplicate. The results were analyzed and represented with a 95% confidence level (p < 0.05). Bars in the graphs represent the mean ± standard deviation.

Page 9 of 33 Nanoscale

#### 2.2. Relative performance of the coatings: weight loss, Ni dissolution, and sessile cell count

The corrosion rates for dGr/Ni (4.7±0.4 mpy) were 2-fold and 3-fold higher than bare Ni (2.5±0.2 mpy) and biGr/Ni (1.6±0.3 mpy), respectively (see Figure 2a for day 12 results), based on the weight loss measurements. Prolonged exposure to the OA-G20 cells escalated these differences. The corrosion rate of dGr/Ni (9.1±0.4 mpy) on day 24 was 1.7-fold and 2.8-fold higher than bare Ni (5.3±0.3 mpy) and biGr/Ni (3.2±0.3 mpy), respectively. The aggravated behavior of dGr/Ni is due to its ability to promote biofilm sessile cell counts (14.3±2 x 10<sup>5</sup> CFU/cm<sup>2</sup>) than bare Ni (13.1±1 x 10<sup>5</sup> CFU/cm<sup>2</sup>) and biGr/Ni (5.6±0.9 x 10<sup>5</sup> CFU/cm<sup>2</sup>) (Figure 2b). The greater the number of sessile cells the greater the degree of electrons harvested from the Ni oxidation. This is evident from the greater Ni<sup>2+</sup> dissolution in dGr/Ni (36.7±4.6 mg/L) which was 1.5-fold and 2.4-fold than bare Ni (24.7±4.6 mg/L) and biGr/Ni (15.6±3.6 mg/L), respectively. This higher dissolution assisted in greater biofilm volume on dGr/Ni (3806±72) μm<sup>3</sup>) than biGr/Ni (1734±335 μm<sup>3</sup>) (Figure 2c). The enhanced metabolic activities of the OA-G20 cells on dGr/Ni are evident from elevated levels of H<sub>2</sub>S (593±35 ppm) which were 1.2-fold and 1.9-fold greater than bare Ni (514±39 ppm) and biGr/Ni (319±30 ppm), respectively (Figure 2c). Conversely, the biGr/Ni that lacked these defects experienced lesser biofilm growth and lower Ni<sup>2+</sup> dissolution. Despite similar physiological conditions (e.g., pH of 7 to 7.4) (Figure 2d), the three systems displayed different behavior.

A unique finding here lies in the greater sessile cell attachment and biofilm volume on dGr/Ni compared to bare Ni. Although bare Ni allows the OA-G20 cells to access the entire surface of bare Ni, it displayed a lower ability to promote cell attachment compared to dGr/Ni. Raman analysis revealed the presence of other defects including armchair defects, Stone-Wales defects, and intervalley defects. However, the influence of these defects on cell attachment is a

Nanoscale Page 10 of 33

complex issue with potential connections at the interplay between electronic properties, surface chemistry, and cellular interactions [39]. Armchair defects, for instance, have been reported to introduce metallic or semiconducting behavior in Gr [40]. This alteration in electronic properties can affect the surface charge distribution [41,42], potentially influencing how biomolecules involved in cell adhesion interact with the Gr surface [43]. Similarly, stone-Wales defects can introduce localized reactive sites on the Gr surface due to their altered electronic structure [44]. These reactive sites could interact with biomolecules or introduce changes in surface chemistry, impacting cell adhesion [45]. Intervalley defects, on the other hand, primarily affect the electronic properties within the Gr lattice [46] and might not directly influence initial cell attachment. However, they could potentially influence electrical signaling between cells once they have attached. Despite these potential connections, a more thorough understanding of how these defects specifically influence the electronic properties and surface chemistry of Gr/Ni surfaces, and the subsequent impact on OA-G20 cell attachment is required. Future studies should employ a combination of experimental techniques and computational modeling to analyze these interactions in more detail.

Page 11 of 33 Nanoscale

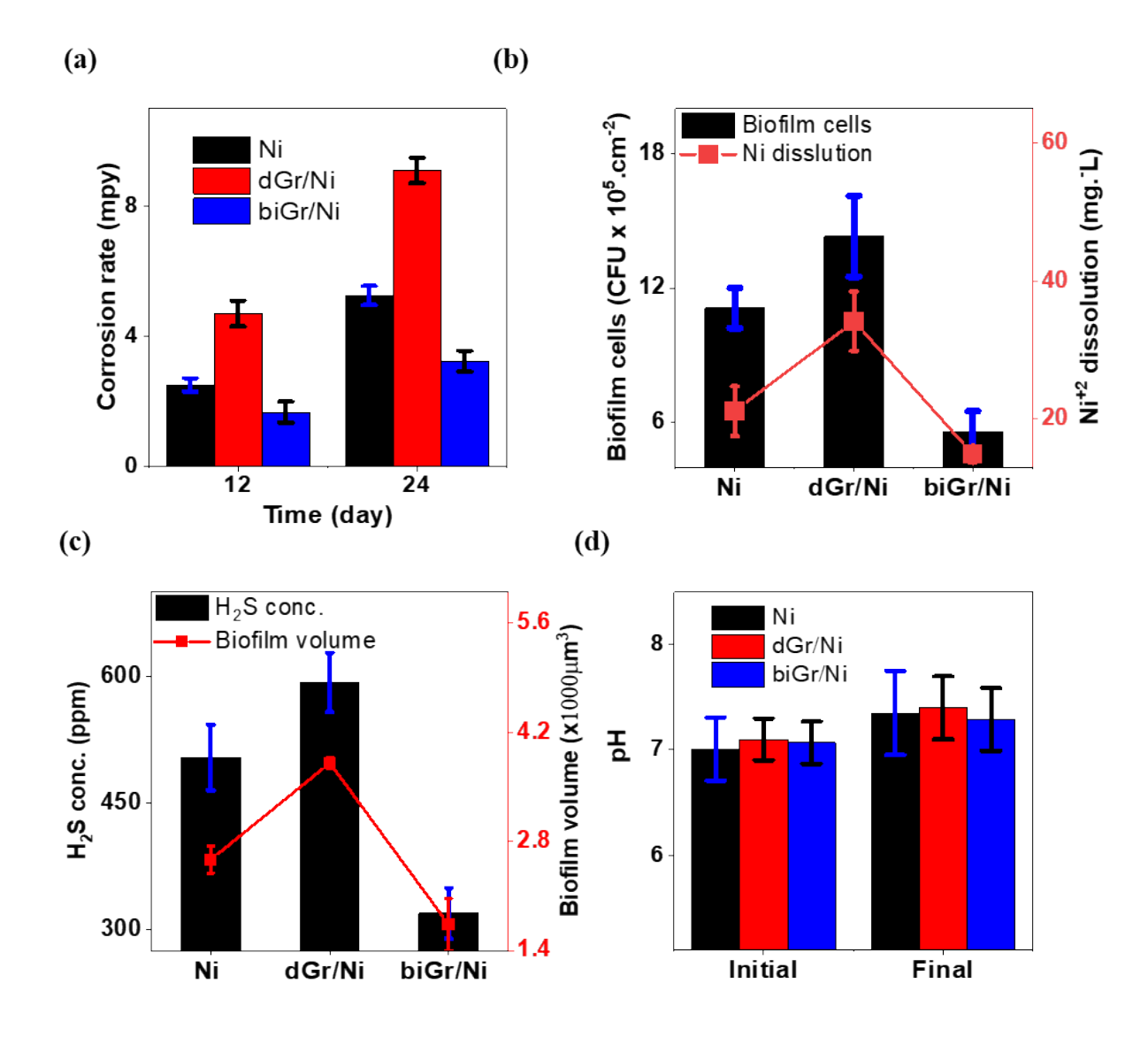


Figure 2. Defect-mediated behavior of Gr/Ni in biological environment. (a) Corrosion rates based on weight loss measurements using 10% H<sub>2</sub>SO<sub>4</sub> (b) Correlation of Ni dissolution with biofilm sessile cells (day 24) (c) Correlation of biofilm volume with H<sub>2</sub>S levels (day 24) (d) pH profiles. Note: Three independent experiments were conducted for each system. The results were analyzed and represented with a 95% confidence level (p < 0.05). Error bars in the graphs represent the mean  $\pm$  standard deviation.

Nanoscale Page 12 of 33

#### 2.3. Electrochemical analysis of defect-mediated biotic corrosion mechanisms

After establishing the differences in performances of dGr/Ni, bare Ni, and biGr/Ni, we turn our attention toward their defect-mediated electrochemical behavior in biological environments (Figure 3). The nobler open circuit potential (OCP) for the bare Ni (-578±36 mV) and biGr/Ni (-560±10 mv) compared to dGr/Ni (-650±38 mV) (Figure 3a) supports the aggravated behavior of dGr/Ni. These larger fluctuations in OCP were attributed to electrochemical activities associated with prolonged microbial exposure, which altered the local environment in terms of pH, microbial metabolites such as exopolysaccharides and H<sub>2</sub>S, and sessile cell count, ultimately resulting in higher anodic dissolution (Fig. 2). This finding is supported by the lower impedance and smaller capacitive loop of dGr/Ni than bare Ni and biGr/Ni (Nyquist plots, Figure 3b). The values of  $|Z|_{0.01~Hz}$  for both dGr/Ni (20 k $\Omega$ .cm<sup>2</sup> to 6  $k\Omega.cm^2$ ) and bare Ni (249  $k\Omega.cm^2$  to 99  $k\Omega.cm^2$ ) dropped after the 24-day exposure, with a greater drop in the former system (Figure S3, Figure S4). However,  $|Z|_{0.01~Hz}$  values of biGr/Ni increased from 57 k $\Omega$ .cm<sup>2</sup> to 104 k $\Omega$ .cm<sup>2</sup> (Figure 3c). These trends were comprehended by the ~7-fold lower  $R_{ct}$  values of dGr/Ni (6.6±0.2 k $\Omega$ .cm<sup>2</sup>) than bare Ni (47±3 k $\Omega$ .cm<sup>2</sup>), based on an equivalent electrical circuit (EEC) analysis (Figure S3, Table S1). The same exposure time showed 2-fold higher  $R_{ct}$  in biGr/Ni (82 $\pm$ 2 k $\Omega$ .cm<sup>2</sup>) than bare Ni on day 24 (Figure 3d).

The range of polarization resistance  $(R_p)$  for dGr/Ni  $(3.2\pm0.3 \text{ to } 2.0\pm0.2 \text{ k}\Omega.\text{cm}^2)$  was significantly lower than bare Ni  $(13\pm1-3\pm0.3 \text{ k}\Omega.\text{cm}^2)$  throughout the test duration. In contrast to these two systems, the biGr/Ni displayed an upward trend  $(4.8\pm0.4-6.3\pm0.1 \text{ k}\Omega.\text{cm}^2)$  (Figure 3e). The aggravated behavior of dGr/Ni was corroborated by observing its higher  $i_{\text{corr}}$  (30±3  $\mu$ A.cm<sup>-2</sup>) which was 2-fold and 3-fold higher than bare Ni  $(15\pm0.2 \mu\text{A.cm}^{-2})$  and biGr/Ni  $(11\pm.2 \mu\text{A.cm}^{-2})$ , respectively (Figure 3f). The inhibition efficiency (IE) of biGr/Ni was 30±2 % while

Page 13 of 33 Nanoscale

that of dGr/Ni showed a negative IE value of -97 $\pm$ 6 %. The IE was derived using  $i_{corr}$  values against bare Ni (Figure 3g, Table S2). The temporal trends for both  $R_p$  and IE corroborated superior corrosion resistance for biGr/Ni and aggravated behavior of dGr/Ni.

The cracks alone in biGr/Ni were not adequate for compromising the barrier properties of Gr coating. Conversely, the partial coverage that featured GBs and edges in dGr/Ni compromised its corrosion resistance (i.e., lowered  $R_{ct}$  values) compared to bare Ni and biGr/Ni respectively (Table S1). The GBs are known to result in decreased work function [9] that allows OA-G20 cells to utilize the energy from the electrochemical gradients along GBs, and thereby decrease the resistance to Faradaic reactions (i.e., decrease  $R_{ct}$  and  $R_p$  in Figure 3) influencing Ni oxidation. Here, we note that the GBs play a unique role in biological environments (relative to abiotic). As shown in Figure S7, the GBs promote corrosion directly by accumulating salt and promoting acid attack. However, in the case of biotic conditions, these GBs exert indirect influence by promoting adherence of the sessile OA-G20 cells onto the underlying Ni surface which in turn promotes the corrosion process (discussed in detail in later sections).

Potentiodynamic polarization plots corroborated the lower corrosion resistance of dGr/Ni than biGr/Ni and bare Ni. Tafel plots indicated a marked shift in cathodic branches of the polarization curves toward higher current densities in dGr/Ni than bare Ni (Figure 3h). The higher cathodic reduction shows greater interactions of the sessile OA-G20 cells with the Ni. [47] Consequently, the Tafel fitting on day 24 indicated a 2.5-fold increase of  $i_{corr}$  in dGr/Ni (8.6  $\mu$ A/cm<sup>2</sup>) compared to bare Ni (3.4  $\mu$ A/cm<sup>2</sup>), while biGr/Ni (1.9  $\mu$ A/cm<sup>2</sup>) inhibited  $i_{corr}$  by 2-fold (Table S3). Cyclic voltammetry (CV) was used to further understand these differences (Figure 3i). The anodic current in dGr/Ni (1.34 A/cm<sup>2</sup>) was 1.5-fold higher than both bare Ni and biGr/Ni, respectively. These results again confirm that the GBs are more adept at promoting cell

Nanoscale Page 14 of 33

attachment and permeation of the oxidizing species <sup>[16]</sup> compared to cracks. The findings on the defect-mediated corrosion behavior of Gr/Ni in biotic environments were compared with abiotic tests using sodium sulfate (SS) and sulfuric acid (SA) electrolytes, respectively (Figure S5, Table S4, Table S5).

Page 15 of 33 Nanoscale

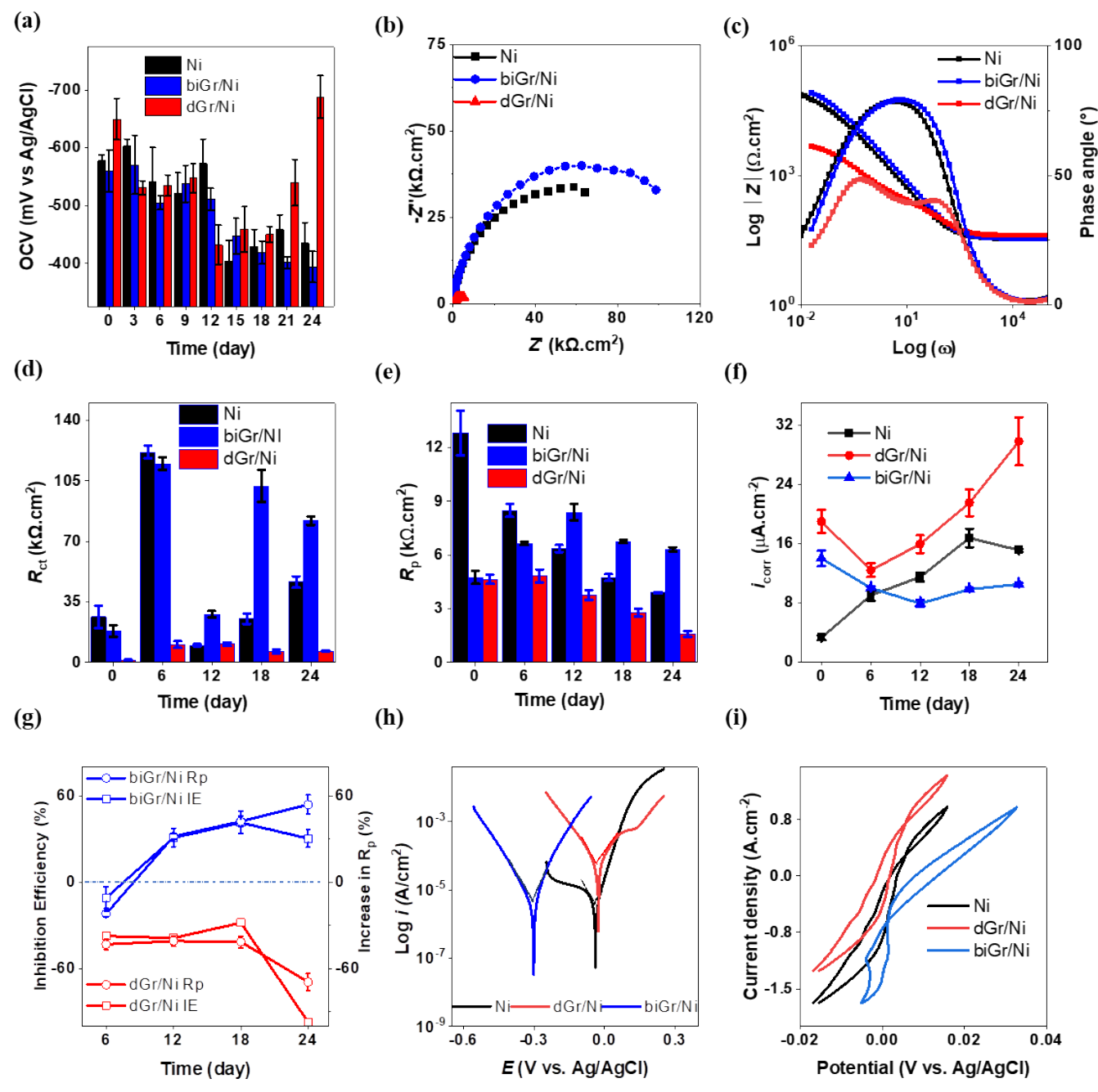


Figure 3. Electrochemical analysis of defect-mediated microbial corrosion performance. Temporal variation of (a) Open circuit potential (b) Nyquist plot for 24<sup>th</sup> day microbial exposure (c) Bode plot on 24<sup>th</sup> day (d) Charge transfer resistance ( $R_{cl}$ ) profiles obtained through EEC (e) Linear polarization resistance ( $R_p$ ) values highlighting the least resistance for dGr/Ni (f) Corrosion current ( $i_{corr}$ ) (g) Inhibition efficiency based on icorr and increase in  $R_p$  values against bare Ni (h) Potentiodynamic polarization plots in a potential range of  $\pm$  250 mV from open circuit voltage (i) Cyclic voltammogram with the scan rate of 0.25 mV/s. Electrochemical impedance spectroscopy was carried out in the frequency range of  $10^{5}\sim10^{-2}$  Hz with an amplitude of 10 mV sinusoidal disturbance. LPR experiments were conducted in triplicate. The results ( $R_p$ ,  $i_{corr}$ ) were analyzed and represented with a 95% confidence level (p < 0.05). Error bars in all the graphs represent the mean  $\pm$  standard deviation.

Nanoscale Page 16 of 33

## 2.4. Surface morphology analysis

We focused on analyzing the ability of the defects to promote the differential formation of OA-G20 biofilms. The abiotic controls devoid of OA-G20 cells did not experience any sign of degradation even after prolonged exposure (Figure 4, Top row). However, the bare Ni and dGr/Ni were blemished by black precipitates (Figure 4a and Figure 4b). These black precipitates observed on Ni and dGr/Ni are likely a result of interactions between the media components in the Lactate-C medium and the sample surfaces. The Lactate-C medium contains various ionic species, including phosphates, sulfates, ammonium, and chlorides [48]. Although similar precipitates were also seen on biGr/Ni, they were loosely attached to the surface. Consequently, these precipitates detached from the biGr/Ni during the removal of the samples from the serum bottle reactors for SEM sample preparation, hence biGr/Ni preserved its pristine surface (Figure 4c). All three systems underwent biogenic sulfide attack when exposed to OA-G20 cells. However, they show a varying degree of degradation based on the weight loss and EIS tests.

The biofilms on bare Ni (Figure 4d), dGr/Ni (Figure 4e), and biGr/Ni (Figure 4f) were distinctly different. The OA-G20 cells showed a preferential adherence towards GBs (Figure 4g, Figure 4h), with a significant biofilm growth observed around the GB regions at the end of the tests (Figure 4e). This preferential behavior manifested in the form of increased sessile cell attachment and greater biofilm volume (Figure 2b, Figure 2c) as well as in the structural damages that featured distinct biogenic sulfide formation (Figure 4i). These findings align with the preferential attacks by acid and salt on GBs under abiotic tests (see Figure S7, S8). Preferential cellular attachment on the GB regions was previously observed for *Pseudomonas* sp. on the bulk stainless steel welds. [49] Overall, the greater degree of GBs and less Gr coverage (reactive Gr edges) in dGr/Ni increased hydrophilicity and roughness and in turn promoted

Page 17 of 33 Nanoscale

attachment of OA-G20 cells and their growth into thicker biofilm compared to bare Ni and biGr/Ni, respectively (Figure 4d-f). Although biGr/Ni experienced occasional colonization, the lack of GBs discouraged biofilm growth (Figure 2c, Figure 4f). Interestingly, the presence of PMMA residues had no impact on bacterial adhesion during the MIC analysis (Figure S1, Figure S9).

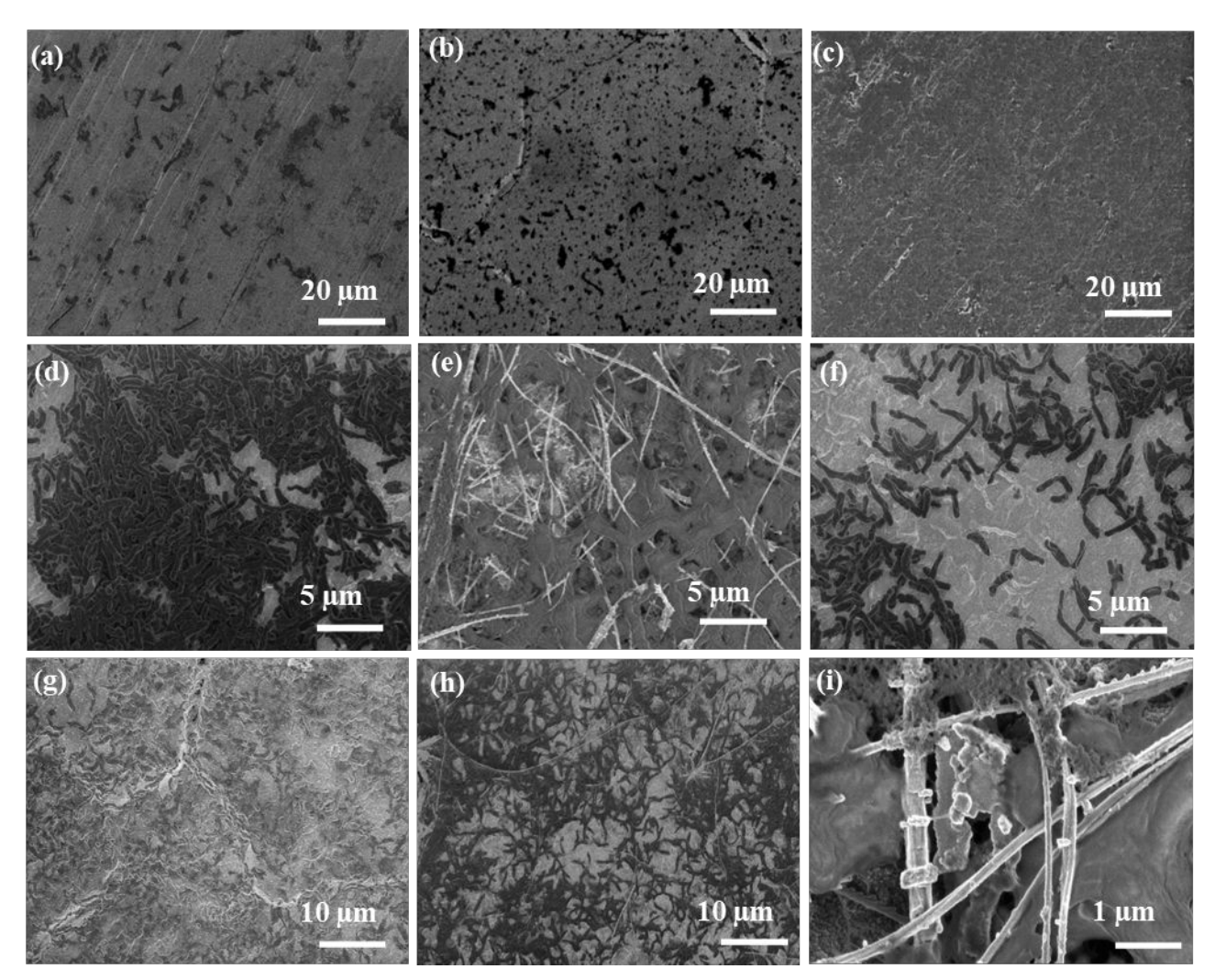


**Figure 4. Optical images of defect-mediated biofilm growth on Gr/Ni. Top row:** SEM images of (a) bare Ni (b) dGr/Ni (c) biGr/Ni exposed to Lactate-C media without OA-G20 cells (abiotic control) for 24 days. Images were obtained with 1.0kV excitation voltage with 1825X magnification using TLD. **Middle row:** SEM images of (d) bare Ni (e) dGr/Ni (f) biGr/Ni exposed to the OA-G20 cells for 24 days. Images were obtained with 1.0kV excitation voltage with 8000X magnification using TLD. **Bottom row:** SEM images of morphological changes and GB mediated corrosion on (g) 8<sup>th</sup> day (h) 16<sup>th</sup> day (i) Distinct forms of biogenic metal sulfide. All images are acquired with 1.0kV excitation voltage with 5000x magnification using a through-the-lens detector (TLD).

Nanoscale Page 18 of 33

## 2.5. Pitting profile and corrosion product analysis

The higher biofilm volume, sessile cell count, and Ni<sup>2+</sup> dissolution in dGr/Ni jointly contributed to pitting corrosion (Figure 5). The CLSM images (Figure 5a-c) revealed that the surface roughness of dGr/Ni (1.8±0.2 µm) experienced a 2-fold greater increase than bare Ni (1.1±0.1 μm) and biGr/Ni (0.8±0.1 μm), respectively (Figure 5d). The rougher the surface the greater the degree of degradation and formation of associated corrosion products (Figure 5 Insets). The average depth of the six largest pits on dGr/Ni, bare Ni, and biGr/Ni were 4.2±0.4 μm, 2.8±0.4 μm, and 1.4±0.2 μm, respectively (Figure 5e). The average pit depth for dGr/Ni was thus 3-fold higher than biGr/Ni. The pit depth at the GBs (5.7±0.6 µm) was 36% larger than the grain region of dGr/Ni. Large pits create localized changes in the electrochemical gradients and associated corrosion products to facilitate access of nutrients (e.g., Ni<sup>+2</sup>) and electron acceptors (e.g., H<sup>+</sup>) to OA-G20 cells, <sup>[50]</sup> hence displaying preferential attachment. The EDS spectrum (see Figure 5g) shows that the corrosion products in the GB regions accumulated a higher content of S and lower O (Figure 5h) while grain regions showed higher O than S (Figure 5i). The interstitial S and O originating from the media components (e.g.,  $SO_4^{2-}$ ) reduce the chemical stability of Gr by creating vacancies that promote the dispersive growth of corrosive reactants.<sup>[51]</sup> Microbially mediated redox reactions of S compounds within biofilms at GBs explain a higher corrosion rate of dGr/Ni than biGr/Ni [52] and higher pitting corrosion. These sulfides induce microvoids and cracks [16] near the GBs and reactive edges of Gr in dGr/Ni. The XRD analysis highlighted the increased presence of nickel sulfide (NiS) on dGr/Ni (Figure S6) than biGr/Ni (Figure 4i, Figure 5f).

Page 19 of 33 Nanoscale

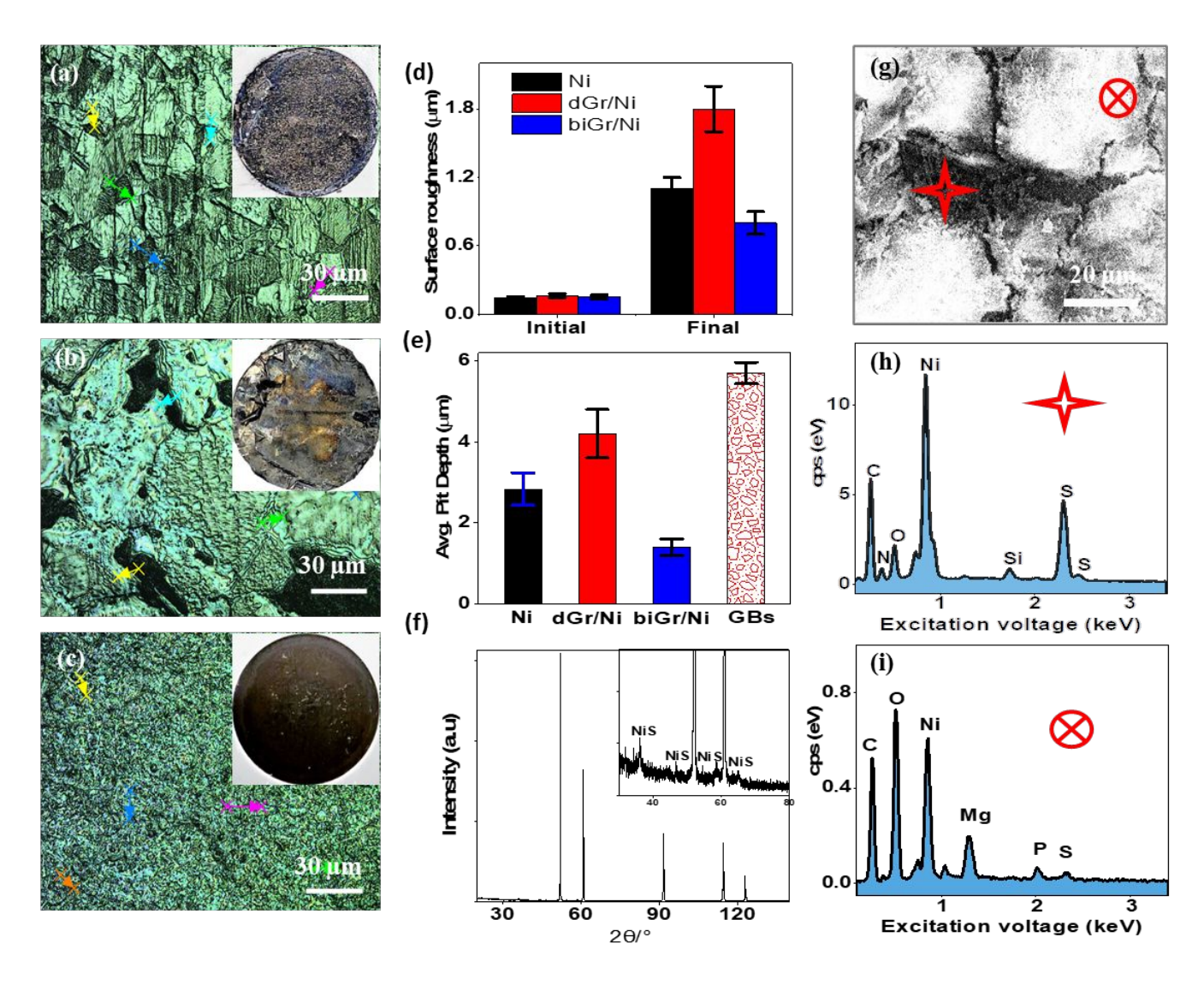


Figure 5. Pitting profile and corrosion products on the exposed regions including GBs. CLSM images showing pitting profile and surface roughness of (a) bare Ni (b) dGr/Ni (c) biGr/Ni (Insets: Visual confirmations of surfaces after 24-day exposure) (d) Surface roughness profiles obtained for unexposed and exposed Ni surfaces (after washing away the OA-G20 sessile cells) (e) Average depth of six largest pits (f) XRD peaks for corrosion products. (g) Regions on dGr/Ni chosen for SEM-EDS analysis (h) SEM-EDS spectra at GB pits of dGr/Ni indicating high S and low O content (i) SEM-EDS spectra at grain region of dGr/Ni indicated high O and very low S content.

Nanoscale Page 20 of 33

## 2.6. Fundamental mechanisms of MIC by nano-to-micron scale defects

Based on the results, we present central mechanisms for the effects of key structural defects on the protection behavior of Gr/Ni in the biotic environment (Figure S10). The defects promote attachment of the OA-G20 cells (Figure 4) that disrupt passivating films  $^{[53]}$  of nickel oxide layers. $^{[54]}$  The attached cells then clear the corrosion pathways (Equations 1-6) to couple Ni<sup>2+</sup> dissolution (Eq. 1) with SO<sub>4</sub>-2 reduction (Eq. 3) ( $\Delta$ Eo'= +33 mV, n=8 @25 °C, pH=7 and 1M solute) and lactate oxidation (Eq. 2), respectively. The obtained energy supports the cell growth of attached cells  $^{[55]}$  and cellular functions (e.g., chemotaxis, $^{[56]}$  metal binding, $^{[57]}$  exopolysaccharide formation.  $^{[58]}$ )

*Ni oxidation (Anodic)* [59]:

$$4Ni \rightarrow 4Ni^{2+} + 8e^{-}$$
 (Eo' = -250 mV) (1)

*Lactate oxidation* [60]:

$$2CH_3CHOHCOO^- + 2H_2O \rightarrow 2CH_3COO^- + 2CO_2 + 8H^+ + 8e^- (E^{o'} = -430 \text{ mV})$$
 (2)

*Sulfate reduction (Cathodic)* [60]:

$$SO_4^{2-} + 9H^+ + 8e^- \rightarrow HS^- + 4H_2O$$
 (Eo' = -217 mV)

Coupling lactate oxidation with sulfate reduction [60]:

$$2\text{CH}_3\text{CHOHCOO}^- + \text{SO}_4^{2-} + \text{H}^+ \rightarrow 2\text{CH}_3\text{COO}^- + 2\text{CO}_2 + \text{HS}^- + \text{OH}^- + \text{H}_2\text{O} \ (\Delta \text{E}^{\text{o}^{\text{t}}} = +213 \text{ mV}) \ (4)$$
  
The sulfate reduction [61] yields HS<sup>-</sup> that reacts with H<sup>+</sup> to form H<sub>2</sub>S gas and escape into the gas

phase (Eq 5).

$$HS^- + H^+ \leftrightharpoons H_2S \tag{5}$$

The GBs result in greater work of adhesion, hydrophilicity (Figure 1f), cell adhesion [49] (Figure 2c), biofilm growth (Figure 4), sessile cell count in dGr/Ni compared to bare Ni and biGr/Ni (Figure 2b, Figure 4). These sessile cells are adept at utilizing the Ni<sup>2+</sup> ions (Eq. 1)

Page 21 of 33 Nanoscale

compared to their planktonic counterparts.<sup>[62]</sup> The edges offer O-containing reactive sites <sup>[63]</sup> that bind the OA-G20 cells with underlying Ni via hydrogen bonding.<sup>[64]</sup> The resulting Ni<sup>2+</sup> ions around the GBs (Figure 2b) (Eq. 1) can promote the expression of Ni-containing hydrogenase enzymes (e.g., [NiFeSe]) <sup>[65]</sup> as well as react rapidly with bisulfide ions <sup>[66]</sup> (Eq. 3) to form NiS (Eq. 6).

$$Ni^{2+} + HS^{-} \rightarrow NiS + H^{+} \tag{6}$$

The crystalline NiS (Eq 6) was prominently found in the GBs (Figure 4i, Figure 5f) showing the SRB-mediated growth.<sup>[67]</sup> The GBs thus constitute conducive sites to promote pitting corrosion (Figure 5d). The high levels of the sulfide ions at these sites (Figure 5h) create local supersaturation zones to form precipitates of metal sulfide <sup>[68]</sup> (NiS in this study) that can reduce the terminal electron acceptors such as H<sup>+ [69]</sup> (Figure 5h). Overall, this set of interrelated events disrupts native Ni oxide passivating layers to cause extensive pitting corrosion (Figure 5e, Figure 5g).

Nanoscale Page 22 of 33

#### 3. Conclusion

Discerning biological insights on the effects of defects can address bottlenecks to developing graphene coatings for biological environments. This study unveiled the effects of graphene islands, edges, grain boundaries, and cracks on the performance of graphene on nickel exposed to sulfate-reducing bacteria. A highlight is the worsened corrosion behavior of nickel when modified with graphene coatings featuring islands and grain boundaries. This behavior was due to the influence of these defects on sessile cell counts, biofilm volume, and the formation of excessive biogenic products (e.g., NiS). Abiotic and biotic tests revealed that the disruption of passivating layers begins at these defective sites to catalyze pitting corrosion. In contrast, the bilayered graphene on nickel (biGr/Ni) free of the grain boundaries offered corrosion resistance. The presence of minor cracks in biGr/Ni did not hinder the ability of graphene to prevent the intercalation of corrosive ions and terminal electron acceptors. These results pave a path for analyzing gene expression patterns, signaling pathways, and regulatory mechanisms of sulfate-reducing bacteria in response to the grain boundaries in graphene on ferromagnetic metals. Such biological insights can guide the design and development of graphene coatings that precisely tune relevant phenotypical responses of technologically relevant bacteria. These findings highlight the critical need for targeted design strategies that address and mitigate these defects to enhance the durability and effectiveness of graphene coatings in combating corrosion in biological settings.

Page 23 of 33 Nanoscale

#### 4. Experimental Section

## 4.1. Chemical vapor deposition

<u>Graphene synthesis</u>: Previously established CVD protocols were used for growing Gr on  $25\mu m$  thick PC-Ni foils (Alfa Aesar, 2 cm  $\times$  2 cm, 99.5% purity). The dGr/Ni samples were obtained from the CVD trials at the Midwest Nano Infrastructure Corridor (MINIC) laboratory, Minnesota Nano Center, University of Minnesota (Section 1. SI).

Graphene Transfer: The CVD-synthesized bilayered Gr sample (TTG200BB) [70] from ACS material (CA, USA) was transferred onto PC-Ni by baking for 20 mins at 100 °C. Polymethyl methacrylate (PMMA) coating was then rinsed off from the biGr/Ni by immersing it in acetone for 30 mins and drying it in air. The PMMA transfer process [71] was also used for transferring as-grown CVD-Gr films from Ni foils onto Si wafer coated with a 90 nm thick SiO<sub>2</sub> layer (SiO<sub>2</sub>/Si) (Graphene Supermarket, NY, USA) for characterization purposes (Section 1. SI).

Graphene Characterization: An XpLora Plus Raman Confocal Microscope (Horiba Scientific, Kyoto, Japan) was used to assess the Gr signatures. The degree of coverage and the island density of Gr on Ni surfaces were characterized using VK-X250 confocal laser scanning microscope (CLSM) (Keyence Corp, Itasca, IL, USA) and Raman methods, respectively [72,73]. Atomic force microscopy (AFM) (Asylum MFP 3D) was used to examine the roughness and GBs morphology. The contact angle measurements were performed using a contact angle goniometer (Model 500, Ramé-hart Instrument Co.) which is configured with DROP-image Advanced v 2.4 software.

Nanoscale Page 24 of 33

- 4.2. Sulfate-reducing bacteria. OA-G20 cultures were grown using Lactate-C media and the growth procedures described in our earlier studies [9]. These cultures were used for the electrochemical tests (see §2.3.1) and weight loss studies (see §2.3.2). The purity of the SRB cultures at the end of the tests was analyzed using the 16s rRNA sequencing methods (see §2, SI).
- 4.3. Weight loss and sessile cell count measurement. Weight loss measurements based on immersion tests were conducted using a modified version of the ASTM G31 protocol <sup>[74]</sup>. These tests used 25μm thick Ni samples with a surface area of 2 in² and exposed to Lactate-C media containing OA-G20 cells. The immersion tests were carried out using 250 mL serum bottle reactors containing 200 mL of the culture media. Samples were harvested on day-12 and 24, cleaned using the 10% H<sub>2</sub>SO<sub>4</sub> (ASTM G1 standards), and air-dried before measuring the final weights <sup>[75]</sup>. The average corrosion rate was calculated by the following equation:

Corrosion rate (mpy) = 
$$\frac{K \times W}{(A \times T \times D)}$$

Where, K - constant (3.45x10<sup>6</sup>), T -time of exposure in hours to the nearest 0.01 h, A - area in cm<sup>2</sup> to the nearest 0.01 cm<sup>2</sup>, W – weight loss in grams, to the nearest 1 mg, D- density in g.cm<sup>-3</sup> (8.91 g.cm<sup>-3</sup>).

Sessile cell counts on the exposed surfaces were quantified by isolating and cultivating them on Lactate-C agar plates (see Section 3, SI)

4.4. Nickel dissolution and hydrogen sulfide measurements. The concentration of Ni<sup>2+</sup> ions in the spent electrolytes was analyzed using an Agilent 7900 Inductively Coupled Plasma Mass Spectrometer (ICP-MS) (Section 3. SI). The levels of hydrogen sulfide (H<sub>2</sub>S) in the reactor headspaces were measured using a Forensics detector (model FD-90A) capable of a range from 0 to 100 ppm with 0.1 ppm resolution. The pH of the electrolyte was monitored using an Orion star

Page 25 of 33 Nanoscale

A215 (Thermoscientific, USA). All tests were conducted at room temperature and anaerobic conditions in triplicate form.

- 4.5. Corrosion tests. Corrosion tests were based on a three-electrode cell configured with a reference electrode (1% silver/silver chloride in 33% water solution of saturated KCl), a graphite plate counter electrode, and working electrodes based on (i) bare PC-Ni (bare Ni), (ii) defective form as grown CVD-Gr on PC-Ni (dGr/Ni) and (iii) transferred form of bilayered CVD-Gr on PC-Ni (biGr/Ni). Abiotic corrosion tests were set up to assess the barrier properties of the coatings using 0.5 M H<sub>2</sub>SO<sub>4</sub> and 0.1M Na<sub>2</sub>SO<sub>4</sub> as electrolytes. The duration of abiotic tests was restricted to 24 h. After establishing the barrier properties in abiotic tests, the coatings were assessed for microbial corrosion tests for 24 d. Lactate-C medium along with OA-G20 (10% v/v) served as the electrolyte. Preparation of axenic cultures was followed using the protocols described in our earlier studies [9]. All the electrochemical tests were performed using a Gamry Reference 600 potentiostat and a 400 mL single-compartment corrosion Para Cell Kit (Part No. 992-80, Gamry Instruments).
- 4.6. Biofilm and corrosion product analysis. The morphology of the samples was evaluated using the Helios 5CX FIB-SEM (Thermo Fisher Scientific, Waltham, MA, USA) which is equipped with Oxford Ultimmax EDS spectroscopy with a sensor size of 100 mm² (Oxford Instruments, Concord, MA, US) and Aztec 5.1 program for analyzing chemical composition. The surface roughness and biofilm volume were evaluated using CLSM. We utilized 10% H<sub>2</sub>SO<sub>4</sub> to remove biofilms and corrosion products on day 24 and pitting profiles were analyzed using CLSM. Biofilm morphology was studied by fixing samples with glutaraldehyde (2.5% in 0.1M cacodylate buffer), serially dehydrated in ethyl alcohol (30%, 50%, 70%, and 100% (v/v)), and examined using an established scanning electron microscope (SEM) protocol. The corrosion

Nanoscale Page 26 of 33

deposits were analyzed using an Ultima-Plus X-ray diffractometer (XRD, Rigaku, Japan) and the data were characterized using Jade 7.5 software.

Page 27 of 33 Nanoscale

## **Electronic Supplementary Information**

Supplementary Information is available.

#### Acknowledgements

We acknowledge the financial support received from the National Science Foundation through RII FEC awards (#1849206, #1920954) and NSF CAREER (#1454102). We are grateful for the assistance provided by the Civil and Environmental Engineering department at the South Dakota Mines. The authors acknowledge the assistance from Drs. Jawahar Raj Kalimuthu (Research Scientist III) and Suvarna N. L. Talluri (Research Scientist III) with the 16s rRNA sequencing and characterization of graphene, respectively.

#### **CRediT** authorship contribution statement

Ramesh Devadig: Conceptualization, Visualization, Validation, Writing. Pawan Sigdel: Validation. Md. Hasan Ur-Rahman: Validation. Pulickel M. Ajayan: Validation. Muhammad M. Rahman: Validation, Writing. Venkataramana Gadhamshetty: Resources, Conceptualization, Supervision, Validation, Project administration, Funding acquisition.

#### **Conflict of Interest**

The authors affirm that they do not possess any known competing financial interests or personal relationships that could have potentially influenced the work reported in the paper.

Nanoscale Page 28 of 33

#### References

- [1] A. G. Olabi, M. A. Abdelkareem, T. Wilberforce, E. T. Sayed, Renewable and Sustainable Energy Reviews 2021, 135, DOI 10.1016/j.rser.2020.110026.
- [2] D. Prasai, J. C. Tuberquia, R. R. Harl, G. K. Jennings, K. I. Bolotin, ACS Nano 2012, 6, 1102. https://doi.org/10.1021/nn203507y
- [3] Y. Bai, T. Xu, X. Zhang, Micromachines (Basel) 2020, 11, DOI 10.3390/mi11010060.
- [4] T. P. Dasari Shareena, D. McShan, A. K. Dasmahapatra, P. B. Tchounwou, Nanomicro Lett 2018, 10, DOI 10.1007/s40820-018-0206-4.
- [5] J. Islam, P. K. Obulisamy, V. K. K. Upadhyayula, A. B. Dalton, P. M. Ajayan, M. M. Rahman, M. Tripathi, R. K. Sani, V. Gadhamshetty, ACS Nano 2023, 17, 137. https://doi.org/10.1021/acsnano.2c05512
- [6] T. R. Nayak, H. Andersen, V. S. Makam, C. Khaw, S. Bae, X. Xu, P. L. R. Ee, J. H. Ahn, B. H. Hong, G. Pastorin, B. Özyilmaz, ACS Nano 2011, 5, 4670. https://doi.org/10.1021/nn200500h
- [7] K. T.sriwong, T. Matsuda, Org Process Res Dev 2022, 26, 1857. https://doi.org/10.1021/acs.oprd.1c00404
- [8] S. Pandit, K. Gaska, R. Kádár, I. Mijakovic, ChemPhysChem 2021, 22, 250. doi: 10.1002/cphc.202000769.
- [9] G. Chilkoor, N. Shrestha, A. Kutana, M. Tripathi, F. C. Robles Hernández, B. I. Yakobson, M. Meyyappan, A. B. Dalton, P. M. Ajayan, M. M. Rahman, V. Gadhamshetty, ACS Nano 2021, 15, 447. https://doi.org/10.1021/acsnano.0c03987
- [10] S. Al-Saadi, R. K. S. Raman, M. R. Anisur, S. Ahmed, J. Crosswell, M. Alnuwaiser, C. Panter, Corros Sci 2021, 182, DOI 10.1016/j.corsci.2021.109299.
- [11] H. Liu, T. Gu, G. Zhang, Y. Cheng, H. Wang, H. Liu, Corros Sci 2016, 102, 93. https://doi.org/10.1016/j.corsci.2015.09.023
- [12] D. Xu, Y. Li, F. Song, T. Gu, Corros Sci 2013, 77, 385. https://doi.org/10.1016/j.corsci.2013.07.044
- [13] S. Ullah, X. Yang, H. Q. Ta, M. Hasan, A. Bachmatiuk, K. Tokarska, B. Trzebicka, L. Fu, M. H. Rummeli, Nano Res 2021, 14, 3756. https://doi.org/10.1007/s12274-021-3345-8
- [14] I. Wlasny, P. Dabrowski, M. Rogala, P. J. Kowalczyk, I. Pasternak, W. Strupinski, J. M. Baranowski, Z. Klusek, Appl Phys Lett 2013, 102. https://doi.org/10.1063/1.4795861
- [15] L. Baraton, Z. He, C. S. Lee, J. L. Maurice, C. S. Cojocaru, Y. H. Lee, D. Pribat, in Carbon Nanostructures, Springer International Publishing, 2012, pp. 1–7. https://doi.org/10.1088/978-0-7503-5143-0
- [16] J. Lei, Y. Hu, Z. Liu, G. J. Cheng, K. Zhao, ACS Appl Mater Interfaces 2017, 9, 11902. https://doi.org/10.1021/acsami.7b01539
- [17] D. W. Boukhvalov, M. I. Katsnelson, Nano Lett 2008, 8, 4374. https://doi.org/10.1021/nl802234n

Page 29 of 33 Nanoscale

- [18] H. C. Wu, Y. Y. Li, A. Sakoda, Int J Hydrogen Energy 2010, 35, 4123. https://doi.org/10.1016/j.ijhydene.2010.02.043
- [19] X. Fan, S. Wagner, P. Schädlich, F. Speck, S. Kataria, T. Haraldsson, T. Seyller, M. C. Lemme, F. Niklaus, Sci Adv 2018, 4, eaar5170. https://doi.org/10.1126/sciadv.aar5170
- [20] E. Auchter, J. Marquez, S. L. Yarbro, E. Dervishi, AIP Adv 2017, 7, DOI 10.1063/1.4986780.
- [21] C. Parra, F. Montero-Silva, R. Henríquez, M. Flores, C. Garín, C. Ramírez, M. Moreno, J. Correa, M. Seeger, P. Häberle, ACS Appl Mater Interfaces 2015, 7, 6430. DOI 10.3390/ma10121406
- [22] A. Dahal, M. Batzill, Nanoscale 2014, 6, 2548. https://doi.org/10.1039/C3NR05279F
- [23] Y. Wu, X. Zhu, W. Zhao, Y. Wang, C. Wang, Q. Xue, J Alloys Compd 2019, 777, 135. https://doi.org/10.1016/j.jallcom.2018.10.260
- [24] C. Allen, S. Aryal, T. Do, R. Gautum, M. M. Hasan, B. K. Jasthi, E. Gnimpieba, V. Gadhamshetty, Front Microbiol 2022, 13, DOI 10.3389/fmicb.2022.1059123.
- [25] R. Devadig, B. D. S. Gurung, E. Gnimpieba, B. Jasthi, V. Gadhamshetty, in 2023 IEEE International Conference on Bioinformatics and Biomedicine (BIBM), IEEE, 2023, pp. 4494–4496. https://doi.org/10.1109/BIBM58861.2023.10385810
- [26] B. D. S. Gurung, R. Devadig, T. Do, V. Gadhamshetty, E. Z. Gnimpieba, in 2022 IEEE International Conference on Bioinformatics and Biomedicine (BIBM), IEEE, 2022, pp. 3602–3604. http://dx.doi.org/10.1109/BIBM55620.2022.9995609
- [27] A. Krishnamurthy, V. Gadhamshetty, R. Mukherjee, Z. Chen, W. Ren, H. M. Cheng, N. Koratkar, Carbon N Y 2013, 56, 45. https://doi.org/10.1016/j.carbon.2012.12.060
- [28] G. Chilkoor, S. P. Karanam, S. Star, N. Shrestha, R. K. Sani, V. K. K. Upadhyayula, D. Ghoshal, N. A. Koratkar, M. Meyyappan, V. Gadhamshetty, ACS Nano 2018, 12, 2242. https://doi.org/10.1021/acsnano.7b06211
- [29] C. Ferrante, A. Virga, L. Benfatto, M. Martinati, D. De Fazio, U. Sassi, C. Fasolato, A. K. Ott, P. Postorino, D. Yoon, G. Cerullo, F. Mauri, A. C. Ferrari, T. Scopigno, Nat Commun 2018, 9, DOI 10.1038/s41467-017-02508-x.
- [30] F. Withers, S. Russo, M. Dubois, M. F. Craciun, Nanoscale Res Lett 2011, 6, 1. https://doi.org/10.1186/1556-276X-6-526
- [31] A. C. Ferrari, J. Robertson, Phys Rev B 2000, 61, 14095. https://doi.org/10.1103/PhysRevB.61.14095
- [32] L. G. Cançado, M. A. Pimenta, B. R. A. Neves, M. S. S. Dantas, A. Jorio, Phys Rev Lett 2004, 93, DOI 10.1103/PhysRevLett.93.247401.
- [33] Y. You, Z. Ni, T. Yu, Z. Shen, Appl Phys Lett 2008, 93, DOI 10.1063/1.3005599.
- [34] H. Zhou, C. Qiu, F. Yu, H. Yang, M. Chen, L. Hu, Y. Guo, L. Sun, J Phys D Appl Phys 2011, 44, DOI 10.1088/0022-3727/44/18/185404.
- [35] Z. Peng, Z. Yan, Z. Sun, J. M. Tour, ACS Nano 2011, 5, 8241. https://doi.org/10.1021/nn202923y

Nanoscale Page 30 of 33

- [36] J. Gao, Q. Yuan, H. Hu, J. Zhao, F. Ding, Journal of Physical Chemistry C 2011, 115, 17695. https://doi.org/10.1021/jp2051454
- [37] S. L. Welsh, M. Kapoor, O. D. Underwood, R. L. Martens, G. B. Thompson, J. L. Evans, J Mater 2016, 2016, 1. https://doi.org/10.1007/s13632-016-0306-9
- [38] A. I. Aria, P. R. Kidambi, R. S. Weatherup, L. Xiao, J. A. Williams, S. Hofmann, Journal of Physical Chemistry C 2016, 120, 2215. https://doi.org/10.1021/acs.jpcc.5b10492
- [39] G. T. Leuthner, T. Susi, C. Mangler, J. C. Meyer, J. Kotakoski, 2d Mater 2021, 8, 035023. DOI 10.1088/2053-1583/abf624
- [40] H. Zheng, Z. F. Wang, T. Luo, Q. W. Shi, J. Chen, Physical Review B—Condensed Matter and Materials Physics 2007, 75, 165414. https://doi.org/10.1103/PhysRevB.75.165414
- [41] R. S. K. Houtsma, J. de la Rie, M. Stöhr, Chem Soc Rev 2021, 50, 6541. DOI: 10.1039/D0CS01541E
- [42] F. Cervantes-Sodi, G. Csányi, S. Piscanec, A. C. Ferrari, Physical Review B—Condensed Matter and Materials Physics 2008, 77, 165427. https://doi.org/10.1103/PhysRevB.77.165427
- [43] W. Qin, X. Li, W.-W. Bian, X.-J. Fan, J.-Y. Qi, Biomaterials 2010, 31, 1007. https://doi.org/10.1016/j.biomaterials.2009.10.013
- [44] M. Tang, Z. Yuan, J. Sun, X. Sun, Y. He, X. Zhou, Model Simul Mat Sci Eng 2023, 32, 015008. DOI 10.1088/1361-651X/ad0a41
- [45] S. Masroor, Functionalized Carbon Nanotubes for Biomedical Applications 2023, 1. https://doi.org/10.1002/9781119905080.ch1
- [46] A. R. Botello-Méndez, X. Declerck, M. Terrones, H. Terrones, J.-C. Charlier, Nanoscale 2011, 3, 2868. https://doi.org/10.1039/C0NR00820F
- [47] A. Abdullah, N. Yahaya, M. N. Norhazilan, R. M. Rasol, J Chem 2014, 2014, DOI 10.1155/2014/130345.
- [48] R. K. Sani, G. Geesey, B. M. Peyton, Advances in Environmental Research 2001, 5, 269. https://doi.org/10.1016/S1093-0191(00)00061-7
- [49] K. R. Sreekumari, K. Nandakumar, Y. Kikuchi, Biofouling 2001, 17, 303. https://doi.org/10.1080/08927010109378490
- [50] H. C. Qian, W. W. Chang, T. Y. Cui, Z. Li, D. W. Guo, C. T. Kwok, L. M. Tam, D. W. Zhang, Corros Sci 2021, 191, DOI 10.1016/j.corsci.2021.109751.
- [51] M. A. Krishnan, K. S. Aneja, A. Shaikh, S. Bohm, K. Sarkar, H. L. M. Bohm, V. S. Raja, RSC Adv 2018, 8, 499. https://doi.org/10.1039/C7RA10167H
- [52] B. J. Little, R. I. Ray, R. K. Pope, Corrosion 2000, 56. https://doi.org/10.5006/1.3280548
- [53] M. Iida, T. Ohtsuka, Corros Sci 2007, 49, 1408. https://doi.org/10.1016/j.corsci.2006.08.002
- [54] E. Sikora, D. D. Macdonald, Electrochim Acta 2002, 48, 69. https://doi.org/10.1016/S0013-4686(02)00552-2

Page 31 of 33 Nanoscale

- [55] R. K. Thauer, E. Stackebrandt, A. W. Hamilton, in Sulphate-Reducing Bacteria: Environmental and Engineered Systems, Cambridge University Press, 2007, pp. 1–38. https://doi.org/10.1017/CBO9780511541490.002
- [56] F. A. Lopes, P. Morin, R. Oliveira, L. F. Melo, Colloids Surf B Biointerfaces 2005, 46, 127. https://doi.org/10.1016/j.colsurfb.2005.07.020
- [57] J. W. Moreau, P. K. Weber, M. C. Martin, B. Gilbert, I. D. Hutcheon, J. F. Banfield, Science (1979) 2007, 316, 1600. https://doi.org/10.1126/science.1141064
- [58] F. Bou-Abdallah, T. R. Giffune, Biochim Biophys Acta Gen Subj 2016, 1860, 879. doi: 10.1016/j.bbagen.2015.11.005
- [59] Y. Pu, Y. Tian, S. Hou, W. Dou, S. Chen, Npj Mater Degrad 2023, 7, DOI 10.1038/s41529-023-00325-w.
- [60] D. Xu, T. Gu, Int Biodeterior Biodegradation 2014, 91, 74. https://doi.org/10.1016/j.ibiod.2014.03.014
- [61] H. C. Helgeson, Am J Sci 1969, 267, 729. DOI: 10.2475/ajs.267.7.729
- [62] Y. Li, D. Xu, C. Chen, X. Li, R. Jia, D. Zhang, W. Sand, F. Wang, T. Gu, J Mater Sci Technol 2018, 34, 1713. https://doi.org/10.1016/j.jmst.2018.02.023
- [63] P. A. Denis, F. Iribarne, Journal of Physical Chemistry C 2013, 117, 19048. https://doi.org/10.1021/jp4061945
- [64] W. Pajerski, J. Duch, D. Ochonska, M. Golda-Cepa, M. Brzychczy-Wloch, A. Kotarba, Materials Science and Engineering C 2020, 113, DOI 10.1016/j.msec.2020.110972.
- [65] B. Anandkumar, R. P. George, S. Maruthamuthu, N. Parvathavarthini, U. K. Mudali, Corrosion Reviews 2016, 34, 41. https://doi.org/10.1515/corrrev-2015-0055
- [66] R. T. Wilkin, D. A. Rogers, Environmental Chemistry 2010, 7, 514. https://doi.org/10.1071/EN10076
- [67] J. Sitte, K. Pollok, F. Langenhorst, K. Küsel, Geomicrobiol J 2013, 30, 36. https://doi.org/10.1080/01490451.2011.653082
- [68] G. Southam, D. R. Lovley, American Society for Microbiology, Washington DC 2000, 257.
- [69] B. W. A. Sherar, P. G. Keech, D. W. Shoesmith, Corros Sci 2013, 77, 257. https://doi.org/10.1016/j.corsci.2013.08.011
- [70] Y. Lee, S. Bae, H. Jang, S. Jang, S. E. Zhu, S. H. Sim, Y. Il Song, B. H. Hong, J. H. Ahn, Nano Lett 2010, 10, 490. https://doi.org/10.1021/nl903272n
- [71] A. Reina, H. Son, L. Jiao, B. Fan, M. S. Dresselhaus, Z. F. Liu, J. Kong, Journal of Physical Chemistry C 2008, 112, 17741. https://doi.org/10.1021/jp807380s
- [72] X. Li, C. W. Magnuson, A. Venugopal, J. An, J. W. Suk, B. Han, M. Borysiak, W. Cai, A. Velamakanni, Y. Zhu, L. Fu, E. M. Vogel, E. Voelkl, L. Colombo, R. S. Ruoff, Nano Lett 2010, 10, 4328. https://doi.org/10.1021/nl101629g

Nanoscale Page 32 of 33

- [73] B. Huet, J. P. Raskin, Chemistry of Materials 2017, 29, 3431. https://doi.org/10.1021/acs.chemmater.6b04928
- [74] A. NACE, ASTM International, West Conshohocken, PA 2012. https://doi.org/10.1520/G0031-72R04
- [75] A. Gl, ASTM international. lggg 2003. https://doi.org/10.1520/G0001-03R17E01

Page 33 of 33 Nanoscale

**Data and Materials Availability.** The data that support the findings of this study are available from the corresponding author. There are no restrictions on materials.